Supplementary Materials

Simulation-augmented learning for ballistic performance prediction of ultra-high-strength steel

Qichao Wei[1], Pingluo Zhao[1,2,3,*], Qiang Hao[1], Wuguo Chen[4], Hongmei Zhang[1,2,3], Yangwei Wang[1,2,3], Xingwang Cheng[1,2,3,*]

[1]National Key Laboratory of Science and Technology on Materials Under Shock and Impact, School of Materials Science and Engineering, Beijing Institute of Technology, Beijing 100081, China.
[2]Materials Intelligent Innovation Laboratory, Beijing Institute of Technology, Zhuhai 519088, Guangdong, China.
[3]Tangshan Research Institute, Beijing Institute of Technology, Tangshan 063000, Hebei, China.
[4]Institute of Equipment Lightweighting, Beijing Institute of Technology Chongqing Innovation Center, Chongqing 401120, China.

[*]**Correspondence to:** Dr. Pingluo Zhao, Prof. Xingwang Cheng, National Key Laboratory of Science and Technology on Materials Under Shock and Impact, School of Materials Science and Engineering, Beijing Institute of Technology, Beijing 100081, China. E-mail: zhaopingluo@bit.edu.cn; chengxw@bit.edu.cn

Supplementary Table 1. Heat treatment process design and expected primary microstructure details

ID	Heat Treatment Process	Expected Primary Microstructure
1	900℃/1h+OQ	Martensite
2	1000℃/1h+OQ	
3	1100℃/1h+OQ	
4	850°C/1h+OQ+200°C/2h+AC	Tempered Martensite
5	900°C/1h+OQ+200°C/2h+AC	
6	900°C/1h+OQ+400°C/2h+AC	Tempered Martensite, Troostite
7	900°C/1h+OQ+600°C/2h+AC	Tempered Martensite, Sorbite
8	950°C/1h+OQ+200°C/2h+AC	Tempered Martensite
9	1000°C/1h+OQ+200°C/2h+AC	
10	1000°C/1h+OQ+400°C/2h+AC	Tempered Martensite, Troostite
11	1000°C/1h+OQ+600°C/2h+AC	Tempered Martensite, Sorbite
12	1050°C/1h+OQ+200°C/2h+AC	Tempered Martensite
13	1100°C/1h+OQ+200°C/2h+AC	
14	1100°C/1h+OQ+400°C/2h+AC	Tempered Martensite, Troostite
15	1100°C/1h+OQ+600°C/2h+AC	Tempered Martensite, Sorbite
16	1100℃/1h+355℃/30h+OQ	Upper Bainite
17	1100℃/1h+345℃/30h+OQ	
18	1100℃/1h+265℃/10h+OQ	Lower Bainite
19	1100℃/1h+255℃/10h+OQ	
20	1100℃/1h+265℃/20h+OQ	
21	1100℃/1h+265℃/30h+OQ	
22	900℃/1h+265℃/10h+OQ	
23	900℃/1h+265℃/20h+OQ	
24	1000℃/1h+265℃/10h+OQ	
25	1000℃/1h+265℃/20h+OQ	
26	850℃/1h+OQ+-73℃/1h+200℃/2h+AC	Tempered Martensite
27	900℃/1h+OQ+-73℃/1h+200℃/2h+AC	
28	950℃/1h+OQ+-73℃/1h+200℃/2h+AC	

ID	Heat Treatment Process	Expected Primary Microstructure
29	1000℃/1h+OQ+-73℃/1h+200℃/2h+AC	
30	1050℃/1h+OQ+-73℃/1h+200℃/2h+AC	
31	1100℃/1h+OQ+-73℃/1h+200℃/2h+AC	
32	1100℃/1h+OQ+-73℃/1h+260℃/2h+AC	
33	1100℃/1h+OQ+-73℃/1h+300℃/2h+AC	Tempered Martensite, Troostite
34	1100℃/1h+OQ+-73℃/1h+400℃/2h+AC	
35	1100℃/1h+OQ+-73℃/1h+400℃/5h+AC	
36	1100℃/1h+OQ+-73℃/1h+482℃/2h+AC	
37	1100℃/1h+OQ+-73℃/1h+482℃/5h+AC	
38	1100℃/1h+OQ+-73℃/1h+500℃/2h+AC	
39	1100℃/1h+OQ+-73℃/1h+560℃/2h+AC	Tempered Martensite, Sorbite
40	1100℃/1h+OQ+-73℃/1h+560℃/5h+AC	
41	1100℃/1h+OQ+-73℃/1h+600℃/2h+AC	
42	1100℃/1h+OQ+-73℃/1h+700℃/2h+AC	
43	900℃/1h+OQ+-73℃/1h+260℃/2h+AC	Tempered Martensite, Troostite
44	900℃/1h+OQ+-73℃/1h+300℃/2h+AC	
45	900℃/1h+OQ+-73℃/1h+400℃/2h+AC	
46	900℃/1h+OQ+-73℃/1h+400℃/5h+AC	
47	900℃/1h+OQ+-73℃/1h+482℃/2h+AC	
48	900℃/1h+OQ+-73℃/1h+482℃/5h+AC	
49	900℃/1h+OQ+-73℃/1h+500℃/2h+AC	Tempered Martensite, Sorbite
50	900℃/1h+OQ+-73℃/1h+560℃/2h+AC	
51	900℃/1h+OQ+-73℃/1h+560℃/5h+AC	
52	900℃/1h+OQ+-73℃/1h+600℃/2h+AC	
53	900℃/1h+OQ+-73℃/1h+700℃/2h+AC	
54	1100℃/15h+FC	
55	1050℃/15h+FC	
56	1000℃/15h+FC	Pearlite
57	950℃/1h+FC	
58	900℃/1h+FC	

ID	Heat Treatment Process	Expected Primary Microstructure
59	850℃/1h+FC	
60	850℃/1h+WQ+610℃/5h+AC	Tempered Martensite, Sorbite
61	790℃/5h+FC	Pearlite
62	730℃/5h+FC	
63	670℃/5h+FC	
64	850℃/1h+AC	
65	850℃/1h+WQ	Martensite
66	1000℃/1h+WQ	
67	1100℃/1h+WQ	
68	900℃/1h+WQ	
69	900°C/1h+WQ+200°C/2h+AC	Tempered Martensite
70	900°C/1h+WQ+400°C/2h+AC	Tempered Martensite, Troostite
71	900°C/1h+WQ+600°C/2h+AC	Tempered Martensite, Sorbite
72	1000°C/1h+WQ+200°C/2h+AC	Tempered Martensite
73	1000°C/1h+WQ+400°C/2h+AC	Tempered Martensite, Troostite
74	1000°C/1h+WQ+600°C/2h+AC	Tempered Martensite, Sorbite
75	1100°C/1h+WQ+200°C/2h+AC	Tempered Martensite
76	1100°C/1h+WQ+400°C/2h+AC	Tempered Martensite, Troostite
77	1100°C/1h+WQ+600°C/2h+AC	Tempered Martensite, Sorbite
78	1100℃/1h+OQ+-73℃/1h+200℃/4h+AC	Tempered Martensite
79	1050℃/1h+OQ+-73℃/2h+200℃/2h+AC	
80	1100℃/1h+OQ+-73℃/2h+200℃/2h+AC	
81	1150℃/1h+OQ+-73℃/1h+200℃/2h+AC	
82	1150℃/1h+OQ+-73℃/2h+200℃/2h+AC	
83	1050℃/1h+OQ+-73℃/1h+200℃/4h+AC	
84	1150℃/1h+OQ+-73℃/2h+200℃/4h+AC	
85	850℃/1h+WQ+150℃/5h+AC	
86	850℃/1h+WQ+200℃/5h+AC	
87	850℃/1h+WQ+250℃/5h+AC	
88	850℃/1h+WQ+350℃/5h+AC	Tempered Martensite, Troostite

ID	Heat Treatment Process	Expected Primary Microstructure
89	850℃/1h+WQ+400℃/5h+AC	
90	850℃/1h+WQ+450℃/5h+AC	
91	850℃/1h+WQ+500℃/5h+AC	
92	850℃/1h+WQ+600℃/5h+AC	Tempered Martensite, Sorbite
93	850℃/1h+WQ+650℃/5h+AC	
94	790℃/5h+WQ	
95	730℃/5h+WQ	Ferrite + Martensite
96	670℃/5h+WQ	
97	1100℃/1h+OQ+200℃/2h+AC+-73℃/1h+AC	
98	1100℃/1h+OQ+200℃/2h+-73℃/1h+200℃/2h+AC	Tempered Martensite
99	1100℃/1h+OQ+-73℃/1h+200℃/6h+AC	
100	1100℃/1h+OQ+-73℃/1h+200℃/8h+AC	
101	900℃/1h+OQ+300℃/2h+AC	Tempered Martensite, Troostite
102	900℃/1h+OQ+500℃/2h+AC	Tempered Martensite, Sorbite
103	1000℃/1h+OQ+300℃/2h+AC	Tempered Martensite, Troostite
104	1000℃/1h+OQ+500℃/2h+AC	Tempered Martensite, Sorbite
105	1100℃/1h+OQ+300℃/2h+AC	Tempered Martensite, Troostite
106	1100℃/1h+OQ+500℃/2h+AC	Tempered Martensite, Sorbite
107	900℃/1h+WQ+300℃/2h+AC	Tempered Martensite, Troostite
108	900℃/1h+WQ+500℃/2h+AC	Tempered Martensite, Sorbite
109	1000℃/1h+WQ+300℃/2h+AC	Tempered Martensite, Troostite
110	1000℃/1h+WQ+500℃/2h+AC	Tempered Martensite, Sorbite
111	1100℃/1h+WQ+300℃/2h+AC	Tempered Martensite, Troostite
112	1100℃/1h+WQ+500℃/2h+AC	Tempered Martensite, Sorbite
113	1100℃/1h+OQ+-73℃/1h+550℃/2h+AC	Tempered Martensite, Sorbite
114	900℃/0.5h+OQ+200℃/2h+AC	
115	1000℃/0.5h+OQ+200℃/2h+AC	Tempered Martensite
116	1100℃/0.5h+OQ+200℃/2h+AC	
117	1100℃/0.5h+OQ+400℃/2h+AC	Tempered Martensite, Troostite
118	1100℃/0.5h+OQ+-73℃/1h+200℃/2h	Tempered Martensite

ID	Heat Treatment Process	Expected Primary Microstructure
119	1100℃/1h+OQ+200℃/2h+AC+200℃/2h+AC	
120	1100℃/1h+OQ+300℃/2h+AC+300℃/2h+AC	Tempered Martensite, Troostite
121	1100℃/1h+OQ+400℃/2h+AC+400℃/2h+AC	
122	950℃/1h+WQ	Martensite
123	1050℃/1h+WQ	
124	850℃/1h+WQ+550℃/5h+AC	Tempered Martensite, Sorbite
125	700℃/5h+WQ	Martensite
126	1000℃/1h+WQ+150℃/5h+AC	Tempered Martensite
127	1000℃/1h+WQ+200℃/5h+AC	
128	1000℃/1h+WQ+250℃/5h+AC	
129	1000℃/1h+WQ+350℃/5h+AC	Tempered Martensite, Troostite
130	1000℃/1h+WQ+400℃/5h+AC	
131	1000℃/1h+WQ+450℃/5h+AC	
132	1000℃/1h+WQ+500℃/5h+AC	Tempered Martensite, Sorbite
133	1000℃/1h+WQ+600℃/5h+AC	
134	1000℃/1h+WQ+650℃/5h+AC	

Note: AC: Air cooling. OQ: Oil quenching. WQ. Water quenching.

Supplementary Table 2. Mechanical properties dataset of G33 ultra high strength steel

Test Type	Performance Parameter	Units
Quasi-static Tensile Test	Yield Strength	MPa
	Tensile Strength	MPa
	Total Elongation at Fracture	%
Quasi-static Compression Test	Yield Strength	MPa
	Compressive Strength	MPa
Vickers Hardness Test	Vickers Hardness	HRC
Dynamic Tensile Test at 2000/s	Yield Strength	MPa
	Tensile Strength	MPa
	Total Elongation at Fracture	%
Dynamic Compression Test at 3000/s	Yield Strength	MPa
	Compressive Strength	MPa
Dynamic Compression Test at 5000/s	Yield Strength	MPa
	Compressive Strength	MPa

Supplementary Table 3. Service performance dataset of G33 ultra high strength steel

Test Type	Performance Parameter	Unit
G33 Ultra-High Strength Steel Projectile Penetration Test	Penetration Speed	m/s
	Projectile Penetration (Yes/No)	/
	Integrity of Projectile Post-Penetration	/
	Residual Velocity Post-Penetration	m/s
	Critical Projectile Fracture Penetration Velocity	m/s

Supplementary Table 4. Grid parameter definition

param_grid	
n_estimators	100, 200, 500
max_features	Sqrt, 0.5
max_depth	None, 10, 20, 30
min_samples_split	2,5, 10
min_samples_leaf	1, 2, 4

Supplementary Table 5. Initial parameter settings of the MLP regression model

Layer	Parameter	Activation Function
Input Layer	128	ReLU
Hidden Layer	64	ReLU
Output Layer	1	

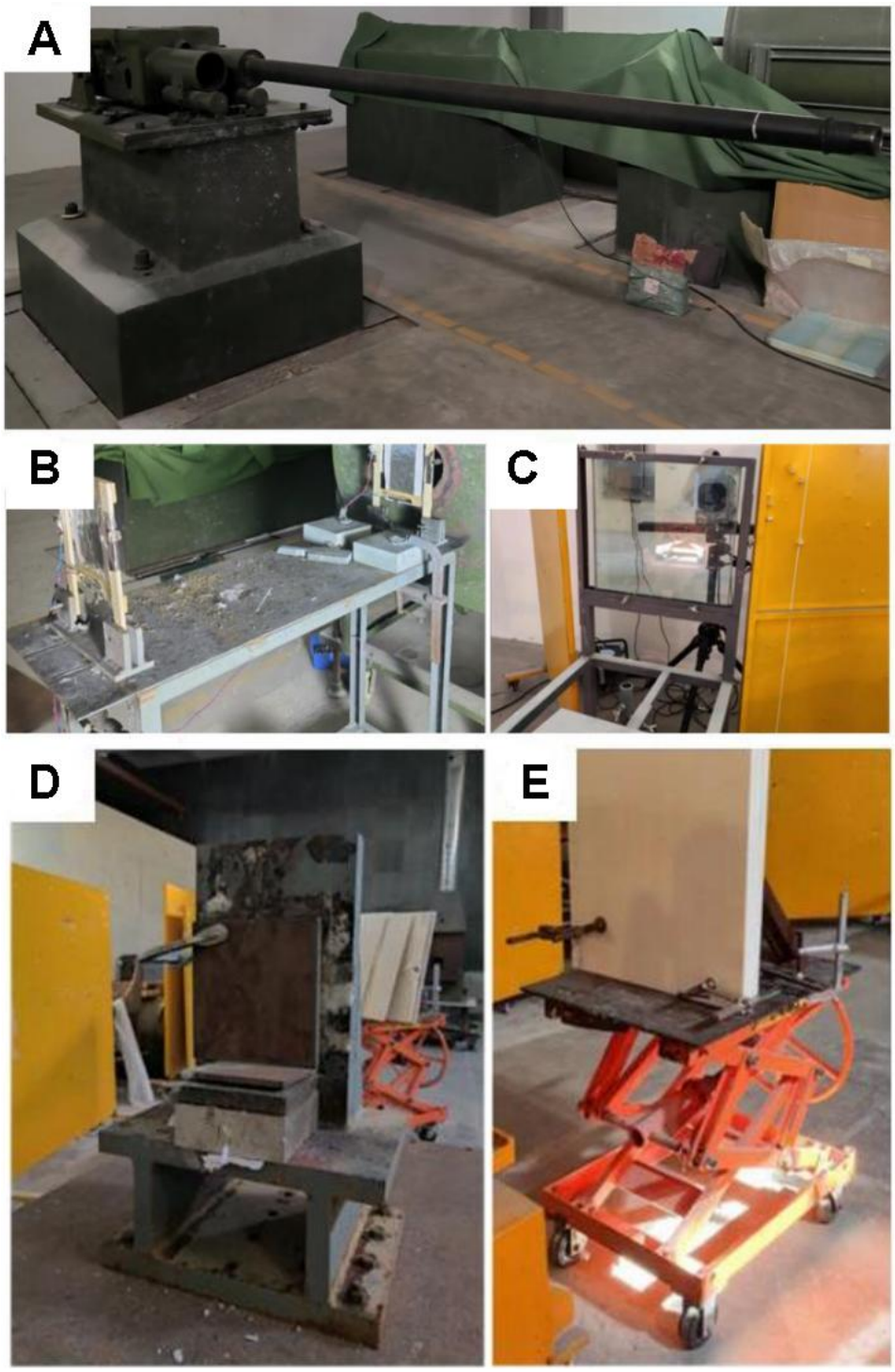

Supplementary Figure 1. (A) 30-37 smoothbore cannon; (B) Foil interrupt target; (C) High-speed camera; (D) Target stand; (E) After-effect target stand and recovery mat(photographs by the authors).

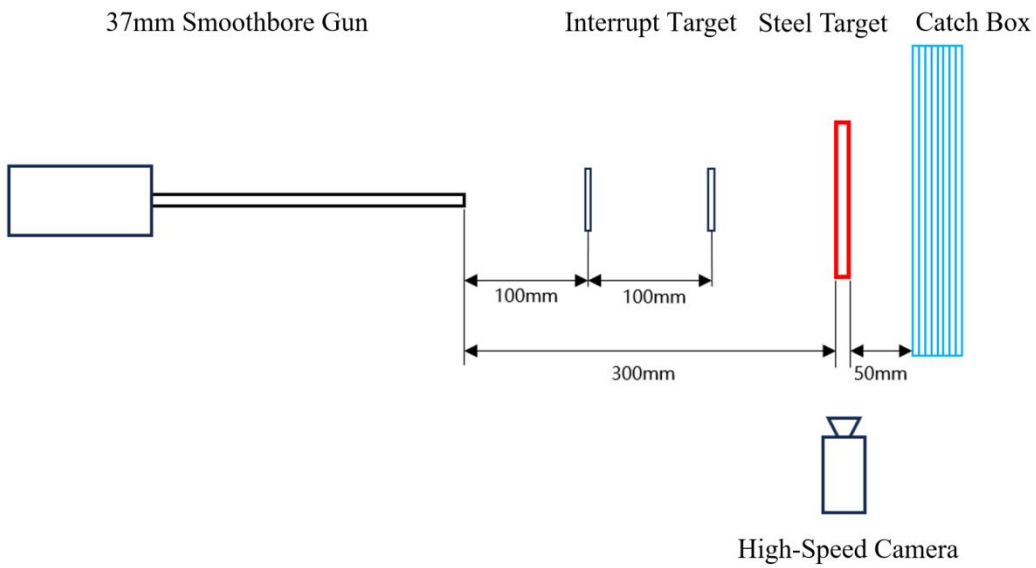

Supplementary Figure 2. Schematic diagram of scaled projectile penetration test.

The dynamic tensile properties of ultra-high-strength steel are accurately determined using a Split Hopkinson Tension Bar (SHTB). Within the SHTB system, both the incident and transmission bars, fabricated from 55CrSi alloy steel, measure 14.5mm in diameter, with lengths of 2000mm and 1000mm respectively. The test specimen, with a gauge section of Φ2×5mm, is securely connected to the loading bars (keyword: *CONTACT_TIDE_SURFACE_TO_SURFACE). To eliminate potential effects from boundary conditions such as the impact velocity on the SHTB loading simulation system, the incident wave recorded during experimental testing is applied as stress at the end face of the incident bar. The loading bars are modeled using a linear elastic constitutive model, while the specimen is described by the Johnson-Cook constitutive and failure model (keyword: *MAT_JOHNSON_COOK). To streamline the computational effort, a quarter-scale model is employed, as depicted in Supplementary Figure 3A.

The quasi-static tensile properties of ultra-high-strength steel are determined using an electronic universal testing machine, with the simulation accurately modeled to reflect the precise dimensions of the actual equipment. The specimen measures a total length of 65mm, including a gauge section 30mm long and 5mm in diameter. Constraints are strategically placed at both ends of the specimen to replicate experimental conditions. Specifically, two layers of elements at one end of the specimen create a robust connection with the loading bar (keyword: *CONTACT_TIDE_SURFACE_TO_SURFACE) and are configured as rigid bodies (keyword: *SECTION_SOLID) to simulate the clamping effects typically provided

by testing fixtures. A single node on the rigid body is set to impose a displacement velocity along the direction of tension (keyword: *BOUNDARY-PRESCRIBED_MOTION_NODE), thus controlling the strain rate of the specimen at 1×10^-3/s. A fixed constraint is also applied at the base of the specimen (keyword: *BOUNDARY_SPC_SET) to emulate the restraint provided by test fixtures during actual experiments. The specimen employs the Johnson-Cook constitutive and failure model (keyword: *MAT_JOHNSON_COOK) for its material characterization. To streamline the computational efforts, a quarter-scale model is employed, as depicted in Supplementary Figure 3B.

To facilitate the automatic extraction of simulation results, the simulation model undergoes specific preprocessing steps. In the Split Hopkinson Tension Bar (SHTB) simulations, circumferential elements at the midpoint between the incident and transmission bars—where resistive strain gauges are typically attached—are designated as a solid element set (keyword: *SET_SOLID). During the simulation, the "stress-time" profiles for these elements along the loading direction are captured and recorded in the elout file (keyword: *DATABASE_HISTORY_SOLID_SET). After the simulation concludes, data from the elout file are extracted to compute the "strain-time" curves for the sets of elements in both the incident and transmission bars. Finally, applying the principles of the three-wave method, the stress-strain curves of the material are calculated.

In simulations of quasi-static tensile tests, two symmetrical nodes are strategically placed along the loading direction on the surface of the specimen (keyword: *SET_NODE_LIST). This setup is intended to replicate the tracking of marked positions by an extensometer during experimental tests. Throughout the simulation, the "position-time" data for these nodes are recorded in the nodeout file. Subsequent extraction and analysis of this data yield the "strain-time" curve for ultra-high-strength steel. Additionally, the last three layers of elements positioned away from the loading direction are grouped into a solid element set (keyword: *SET_SOLID). During the simulation, "stress-time" profiles for these elements are captured in the elout file (keyword: *DATABASE_HISTORY_SOLID_SET). Post-simulation, this data is extracted to compute the "stress-time" curve of the specimen. This analysis culminates in the derivation of the "stress-strain" curve for ultra-high-strength steel under experimental conditions, providing critical insights into material behavior under tensile loading.

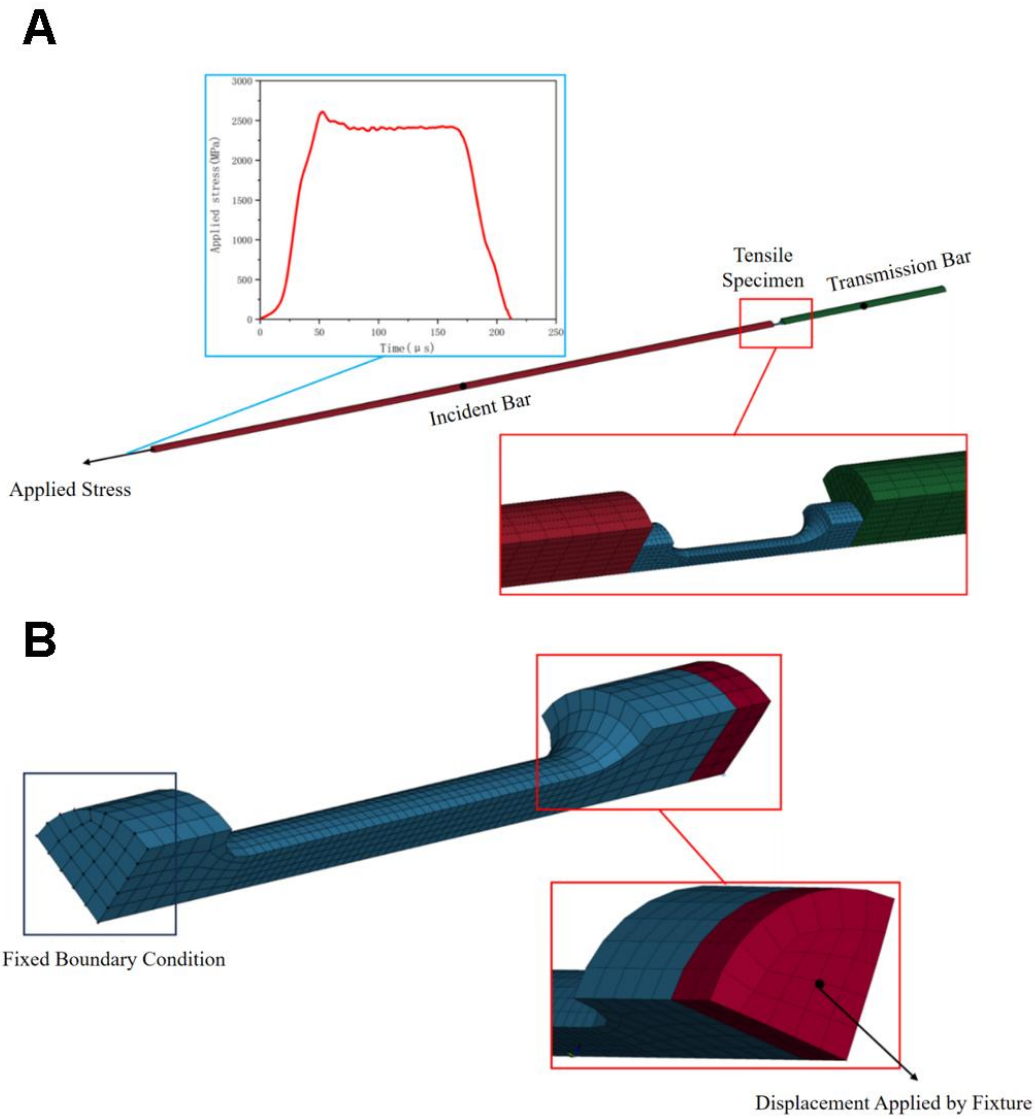

Supplementary Figure 3. (A) Numerical simulation modelof dynamic tensile test; (B) Numerical simulation model of quasi-static tensile test.

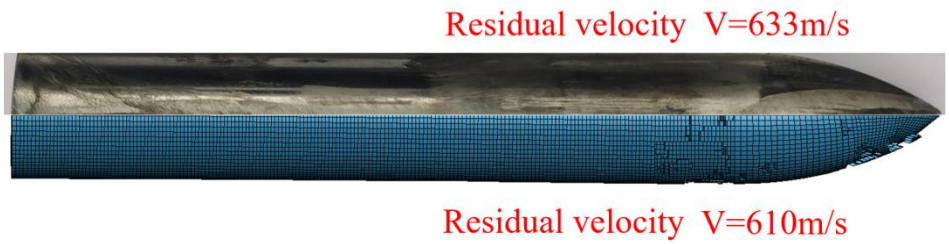

Supplementary Figure 4. Comparison between experimental results and numerical simulation results

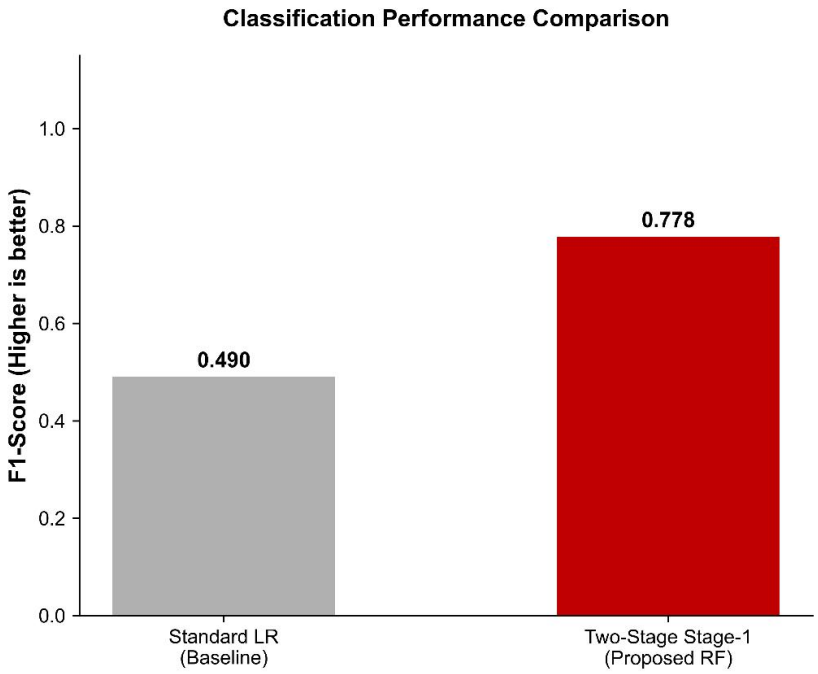

Supplementary Figure 5. Performance comparison of the proposed Two-Stage framework against Single-Stage baselines. Classification F1-score comparison for predicting the ballistic limit boundary (penetration occurrence).

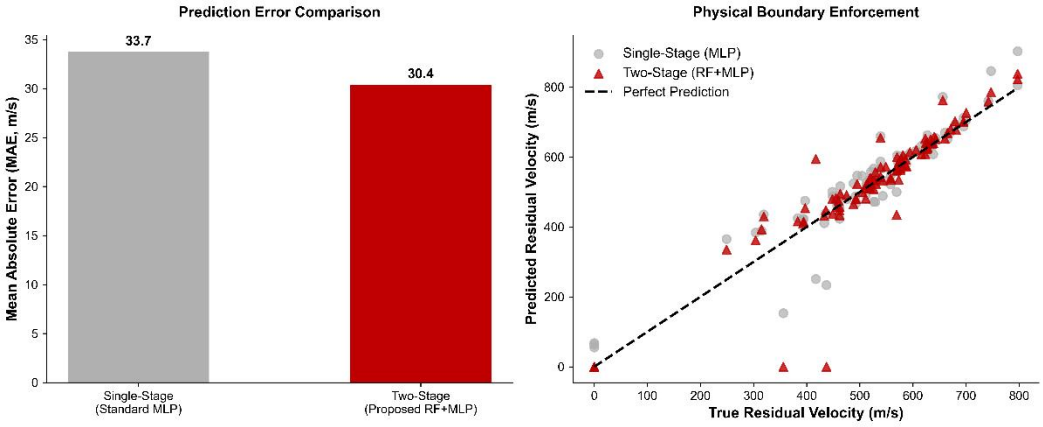

Supplementary Figure 6. Regression Mean Absolute Error (MAE) and physical boundary enforcement for predicting post-failure residual velocity, demonstrating the elimination of zero-boundary anomalies.

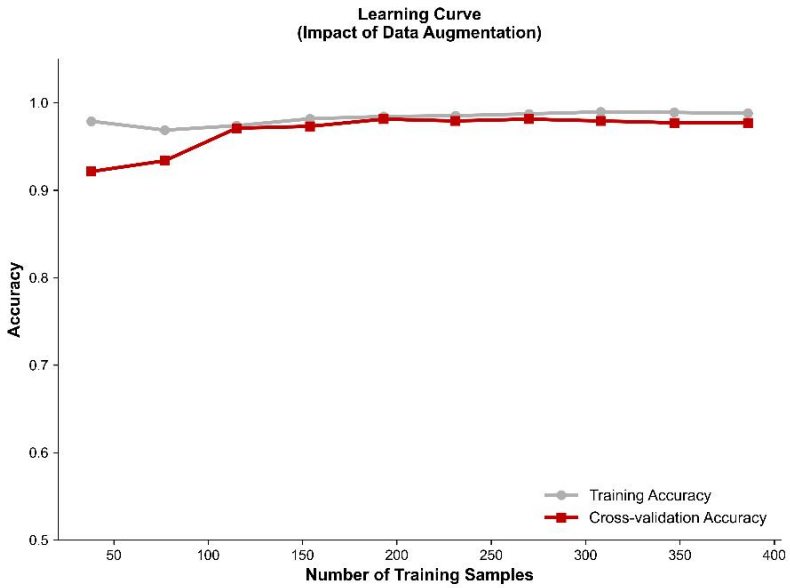

Supplementary Figure 7. Learning curve demonstrating the impact of simulation-based data augmentation. The trajectory of cross-validation accuracy versus training sample size explicitly proves that standard data-driven mappings suffer from underfitting and severe variance under limited initial experimental data (<100 samples), and successfully plateau only after high-throughput simulation augmentation.

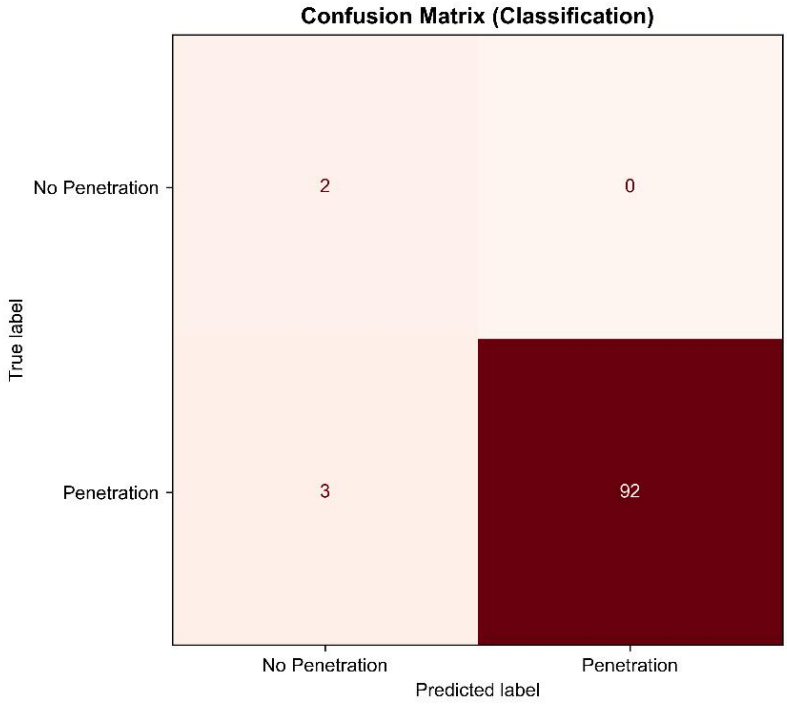

Supplementary Figure 8. Confusion matrix evaluating the predictive accuracy of the Stage-1 Random Forest classifier. The matrix shows a highly balanced and precise classification of the physical threshold (penetration vs. non-penetration) evaluated on the test set.

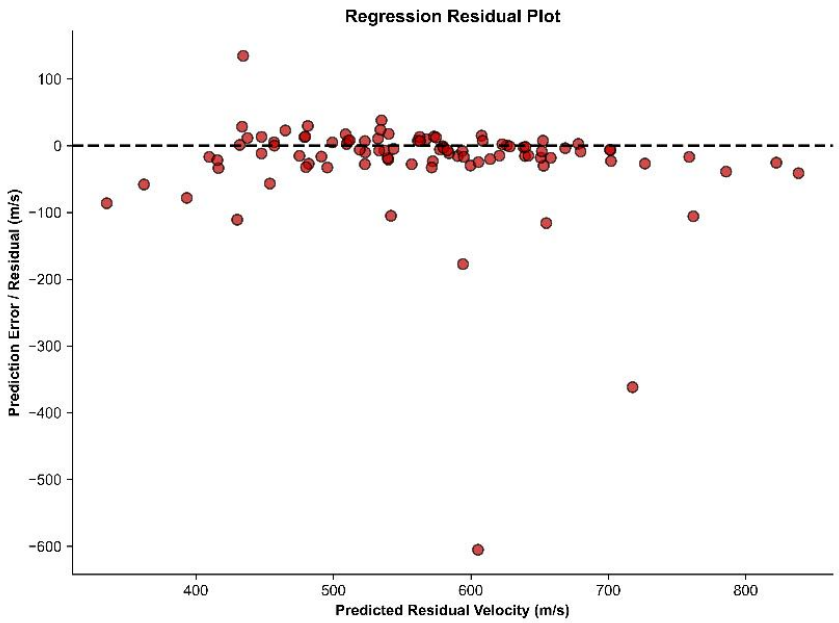

Supplementary Figure 9. Regression residual plot for the Stage-2 MLP model. The plot displays the distribution of prediction errors for penetrated targets, confirming that the residuals are homoscedastic and normally distributed around the zero-error baseline without systematic bias.

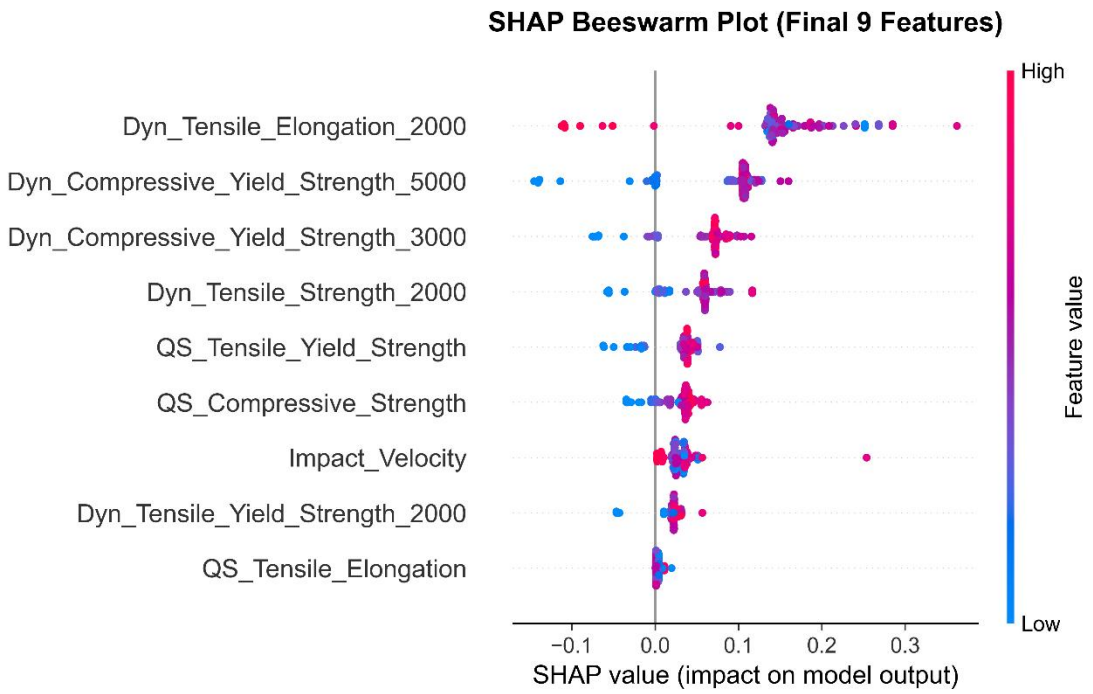

Supplementary Figure 10. SHAP (SHapley Additive exPlanations) summary beeswarm plot illustrating global feature importance. The plot reveals the relative contribution and physical impact directions of various mechanical features on the penetration occurrence, highlighting the dominant roles of impact velocity, dynamic yield strength, and quasi-static elongation.